Resistance of high-temperature cuprate superconductors

2013 New J. Phys. 15 073020

(http://iopscience.iop.org/1367-2630/15/7/073020)

New Journal of Physics
The open access journal for physics

Resistance of high-temperature cuprate superconductors

Jamil Tahir-Kheli
Department of Chemistry, Beckman Institute (MC 139-74), California Institute of Technology, Pasadena CA 91125, USA
E-mail: jamil@caltech.edu

New Journal of Physics **15** (2013) 073020 (22pp)
Received 4 January 2013
Published 9 July 2013
Online at http://www.njp.org/
doi:10.1088/1367-2630/15/7/073020

Abstract. Cuprate superconductors have many different atoms per unit cell. A large fraction of cells (5–25%) must be modified ('doped') before the material superconducts. Thus it is not surprising that there is little consensus on the superconducting mechanism, despite almost 200 000 papers (Mann 2011 *Nature* **475** 280). Most astonishing is that for the simplest electrical property, the resistance, 'despite sustained theoretical efforts over the past two decades, its origin and its relation to the superconducting mechanism remain a profound, unsolved mystery' (Hussey *et al* 2011 *Phil. Trans. R. Soc.* A **369** 1626). Currently, model parameters used to fit normal state properties are experiment specific and vary arbitrarily from one doping to the other. Here, we provide a quantitative explanation for the temperature and doping dependence of the resistivity in one self-consistent model by showing that cuprates are intrinsically inhomogeneous with a percolating metallic region and insulating regions. Using simple counting of dopant-induced plaquettes, we show that the superconducting pairing and resistivity are due to phonons.

Contents

Since superconductivity requires coherent Cooper pairing of electrons, knowing what couples most strongly to electrons is absolutely necessary for understanding what causes high-temperature cuprate superconductivity. The resistivity, the Hall effect and the magnetoresistance (MR) are fundamentally measurements of the momentum dependent Fermi surface scattering rate, $1/\tau(k)$, that measures the strength of whatever is coupling to electrons. If the origin of the scattering rate and its temperature dependence are not understood, then most likely cuprate superconductivity is not understood either.

The earliest resistivity (ρ) measurements [2] on cuprates found ρ to be approximately linear in temperature over the huge temperature range of $10 < T < 1000$ K. A linear T resistivity is characteristic of electron–phonon (or electron–boson) scattering. Yet phonons are not believed to cause ρ, despite the fact that historically, the dominant scattering mechanisms of electrons in metals have been phonons and impurities. There are two reasons for this conclusion: firstly, at low temperatures, the Bose–Einstein statistics of the phonons reduces the phase space for scattering, leading to $\rho(T) \sim T^5$ (the Bloch–Gruneisen law) [3]. The T^5 scaling should be observable for $T < \Theta_{\rm Debye}/10$ where $\Theta_{\rm Debye}$ is the Debye temperature (the characteristic energy of the highest energy phonons). Since $\Theta_{\rm Debye} \sim 400$ K in cuprates [4], phonon scattering is not compatible with the observed linearity. Magnons are also eliminated because $\Theta_{\rm Mag} \sim 1500$ K [5].

Secondly, the magnitude of ρ at high T for some dopings exceeds the Mott–Ioffe–Regel limit (MIR) [6] that occurs when the electron mean free path reaches the shortest Cu—Cu distance ($\approx$3.8 Å). For cuprates, $\rho(T)$ should saturate to $\rho_{\rm MIR} \sim 1000\,\mu\Omega$ cm. Instead, ρ increases linearly right through $\rho_{\rm MIR}$, leading to the conclusion that the normal state may not even be a typical metal (a non-Fermi liquid or 'bad metal') [7].

Both of these conclusions are invalid when the crystal is intrinsically inhomogeneous, as we will show. Briefly, the first point implicitly assumes that phonon momentum is a good quantum number. The second underestimates $\rho_{\rm MIR}$ by overestimating the density of charge carriers [8]. For example, at optimal hole doping of $x = 0.16$ (we define x to be the number of holes per

planar CuO_2), we find the fraction $\approx 4 \times 0.16 = 0.64$ of the crystal is metallic leading to a ρ_{MIR} that is $(1/0.64) = 1.56$ times larger than the conventional estimate. $\rho(T)$ remains below the larger ρ_{MIR} up to the melting temperature.

Recently, the doping and k-vector dependent scattering rate, $1/\tau(x, k)$, has been extracted from a series of beautiful experiments by Hussey *et al* [1, 9–11]. In the first set of experiments [9, 10], the MR of large single crystals of single layer $Tl_2Ba_2CuO_{6+\delta}$ was measured as a function of the direction of an applied 45 tesla magnetic field for $T < 40$ K and large overdoping. They found that $1/\tau(x, k)$ is the sum of three terms, $1/\tau(x, k) = 1/\tau_0(x) + A_1(x)\cos^2(2\varphi)T + A_2(x)T^2$, where $A_1(x)$ and $A_2(x)$ are hole doping dependent constants and φ is the angle between the Cu—O bond direction and the k-vector as shown in the top right corner of figure 6(a). The first term, $1/\tau_0(x)$, is a constant that is sample dependent even at the same doping. The anisotropic linear T term is zero for k-vectors along the diagonal ($\varphi = \pi/4$) and largest for k along the Cu—O bond directions ($\varphi = 0, \pi/2$).

In an elegant theoretical analysis, Hussey *et al* [1, 12, 13] showed that a scattering rate of the above form explained the resistivity, the Hall effect and the MR for a large range of dopings, temperatures and different cuprate materials. The authors suggested that the isotropic T^2 part of the scattering rate arose from electron–electron Coulomb scattering while the origin of the T term is unknown. Finally, the strong doping dependence of $A_1(x)$ and $A_2(x)$ was noted, but not explained.

In another experiment, Hussey *et al* [1, 11] used large magnetic fields to lower the T_c (the superconducting transition temperature) of $La_{2-x}Sr_xCuO_4$. They found that $\rho(T)$ was the sum of doping dependent T and T^2 terms at low temperatures plus a sample and doping dependent constant. These results suggested that the $1/\tau(x, k)$ form found for $Tl_2Ba_2CuO_{6+\delta}$ was applicable to all dopings and cuprate materials.

The authors also found that the low temperature ρ evolved into linear T at high temperatures, as seen previously [14]. They concluded that the isotropic T^2 term was due to electron–electron Coulomb scattering and that MIR saturation of the scattering rate at high temperatures was reducing this term down to linear T.

The experiments described above may be summarized as follows [1]. The temperature derivative of the resistivity, $d\rho(x, T)/dT$, is of the form $d\rho(x, T)/dT = \alpha_1(x, 0) + 2\alpha_2(x)T$ at low temperatures and $d\rho(x, T)/dT = \alpha_1(x, \infty)$ at high temperatures. $\alpha_1(x, 0)$ and $\alpha_1(x, \infty)$ are both doping dependent constants with $\alpha_1(x, 0) < \alpha_1(x, \infty)$ always. ρ smoothly interpolates between these two forms. In addition, $\alpha_1(x, 0)$ is approximately constant for $x < 0.19$ and $\alpha_1(x, \infty)$ is approximately constant for $x > 0.19$. Surprisingly, the low-doping $\alpha_1(x, 0)$ constant and the high-doping $\alpha_1(x, \infty)$ constants appear to be equal ($\approx 1\,\mu\Omega\,\mathrm{cm\,K^{-1}}$) within the experimental error bars. A plot of the experimental data [1] for $\alpha_1(0)$ and $\alpha_1(\infty)$ for $La_{2-x}Sr_xCuO_4$ is shown in figure 1 (for notational convenience, we suppress the x in $\alpha_1(0)$, $\alpha_1(\infty)$, and $1/\tau(k)$ from this point onward).

Even for a fixed doping value, it is clear that the low and high T forms of $1/\tau(k)$ put strong constraints on theory. An even stronger constraint is explaining the doping dependence of $\alpha_1(0)$ and $\alpha_1(\infty)$ and their peculiar 'crossover' at doping of $x \approx 0.19$, as can be seen in figure 1.

In prior publications [15, 16], we showed that cuprates are comprised of a percolating metallic region and insulating regions. The metallic region is formed from four-Cu-site square plaquettes in the CuO_2 planes that may overlap (share a Cu atom). These plaquettes are centered around the dopants (e.g. Sr in $La_{2-x}Sr_xCuO_4$). The insulating regions are comprised of localized d^9 Cu spins that are coupled antiferromagnetically.

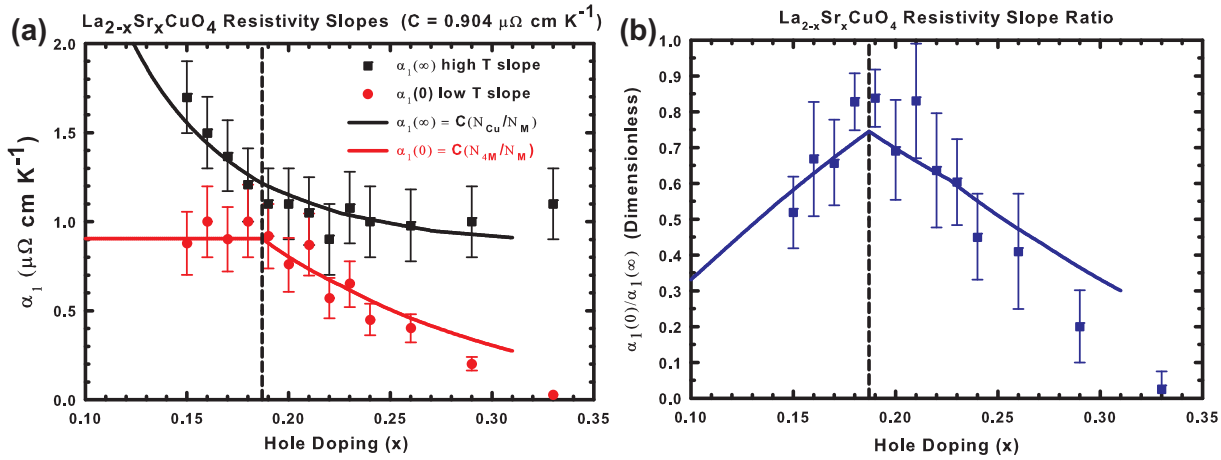

Figure 1. Doping evolution of the linear T coefficients of the resistivity at high and low temperatures ($\alpha_1(0)$ and $\alpha_1(\infty)$). (a) Experiment [1] versus theory. $\alpha_1(0) = C(N_{4M}/N_M)$ and $\alpha_1(\infty) = C(N_{Cu}/N_M)$ where N_M is the total number of metallic Cu sites (yellow in figure 2), N_{4M} is the number of Cu atoms inside the non-overlapping four-Cu-site plaquettes (black squares with the number '4' in figure 2) and N_{Cu} is the total number of planar Cu sites (see figures A.1 and A.2). The low and high temperature linear T scattering rates arise from phonons and are given by $1/\tau(0) \sim N_{4M}T$ and $1/\tau(\infty) \sim N_{Cu}T$, respectively. Dividing by the total number of charge carriers, N_M, leads to $\alpha_1(0)$ and $\alpha_1(\infty)$. For $C = 0.904\,\mu\Omega\,\mathrm{cm\,K^{-1}}$, the RMS and maximum absolute errors are 0.017 and $0.17\,\mu\Omega\,\mathrm{cm\,K^{-1}}$, respectively. (b), Plot of the ratio $\alpha_1(0)/\alpha_1(\infty) = N_{4M}/N_{Cu}$. C cancels out here, so there are zero adjustable parameters. For doping $x < 0.187$, $N_{4M} = N_M$ because there are no overlapping plaquettes. Hence, $\alpha_1(0) = C$. The start of plaquette overlap at $x = 0.187$ (vertical dashed line) leads to the sharp discontinuity in $\alpha_1(0)$ there. Since $N_M \to N_{Cu}$ with increasing doping, $\alpha_1(\infty)$ at high doping tends to the same constant C, as observed. Panels (a) and (b) are the main results of the paper.

By simply counting the volume and surface areas of these two regions as a function of doping, we explained the origin and doping dependence of the pseudogap (PG) [15], the universal room-temperature thermopower, the scanning tunnelling microscopy incommensurability, the neutron resonance peak and the generic cuprate phase diagram [16]. Here, we show that $\alpha_1(0)$ and $\alpha_1(\infty)$ are also explained by the same intrinsic inhomogeneity (figure 2).

We will show that $\alpha_1(0)$ is due to phonon scattering inside non-overlapping plaquettes and $\alpha_1(\infty)$ is due to scattering from all phonons. Therefore, $\alpha_1(0) \propto N_{4M}$ and $\alpha_1(\infty) \propto N_{Cu}$, where N_{4M} equals the number of planar Cu sites inside non-overlapping plaquettes and N_{Cu} is the total number of planar Cu sites. Dividing by the total number of charge carriers, N_M, leads to $\alpha_1(0) = C(N_{4M}/N_M)$ and $\alpha_1(\infty) = C(N_{Cu}/N_M)$. The best fit (see figure 1) is $C = 0.904\,\mu\Omega\,\mathrm{cm\,K^{-1}}$. Figure 1(a) has one adjustable parameter, C. Figure 1(b) is the ratio of $\alpha_1(0)/\alpha_1(\infty)$ and has zero adjustable parameters. The excellent fit in figure 1 using simple counting is the main result of this paper.

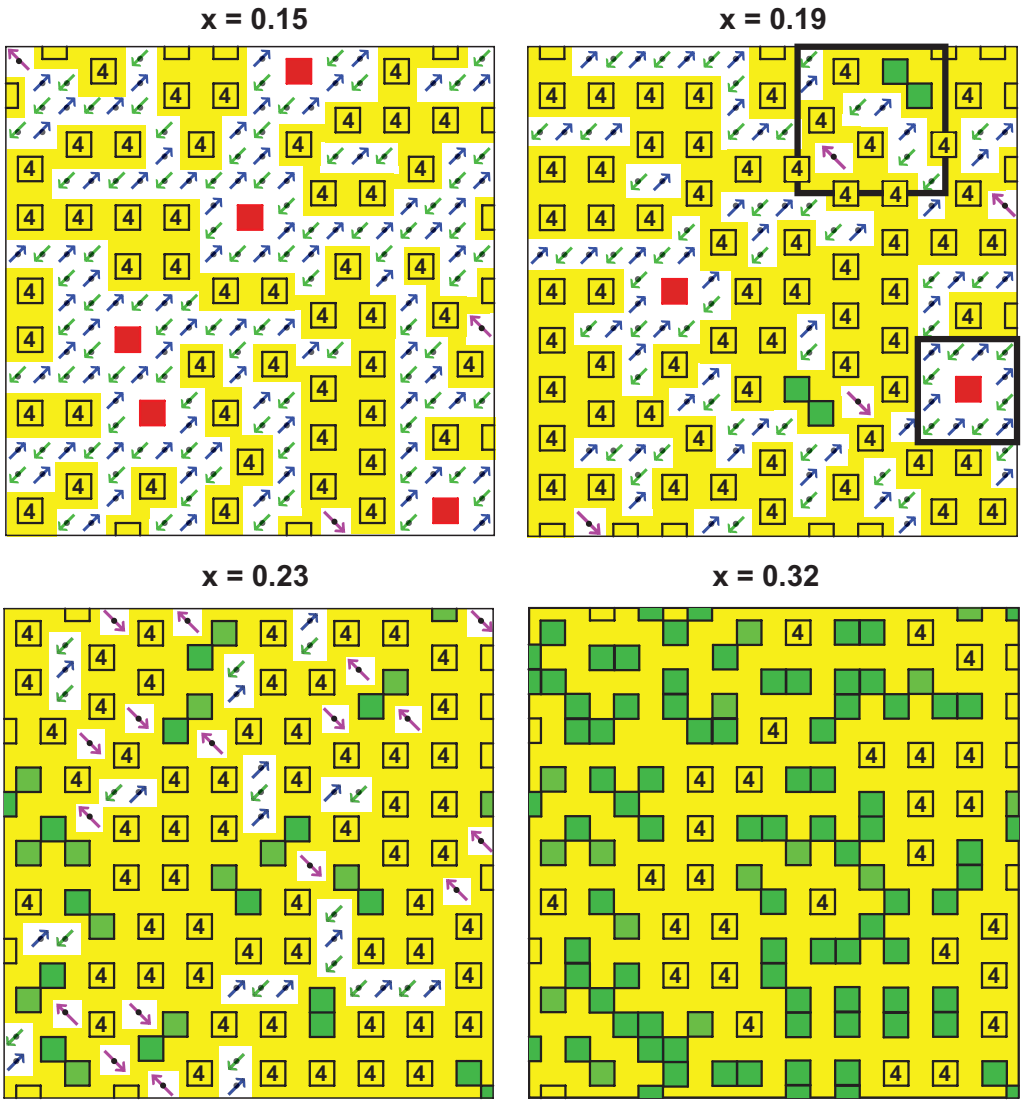

Figure 2. The distribution of plaquettes (non-overlapping and overlapping) on a 20×20 lattice in a single CuO_2 plane. Each black, green, pink, blue and red square represents a plaquette centered at a dopant (Sr in $La_{2-x}Sr_xCuO_4$). The corners of the squares are planar Cu sites. The O atoms are not shown. A Cu $d_{x^2-y^2}$/O p_σ metallic band forms inside the percolating region of the plaquettes and is shown in yellow (see appendix). The non-overlapping plaquettes (black squares with the number '4' inside) will have dynamic Jahn–Teller distortions as shown in figure 3. The number of these amorphous 2D phonon modes is proportional to the number of Cu sites inside these plaquettes, N_{4M}. N_M is the total number of metallic Cu sites (yellow). N_{Cu} is the total Cu sites. Here, $N_{Cu} = 20 \times 20 = 400$. The arrows are undoped d^9 Cu spins that are antiferromagnetically coupled. Plaquettes do not overlap for $x < 0.187$, leading to $N_{4M} = N_M$ (see $x = 0.15$ figure). For $x > 0.187$, overlap is unavoidable (green squares). See Methods section. The red squares are isolated plaquettes with no plaquette neighbors. These plaquettes lead to the PG [15].

Figure 2. (Continued) They are not connected to the percolating 'metallic' swath. The 6×6 black square in the upper right of $x = 0.19$ is expanded in figure 3(c) to show the 2D Jahn–Teller phonon modes and in figure 4 to show the O atom distortions. The 4×4 square in the lower right is expanded in the appendix to show the vicinity of an isolated plaquette (red square).

Figure 2 shows a schematic of the distribution of plaquettes and how N_{4M}, N_M and N_{Cu} are calculated. The insulating/antiferromagnetic (AF) regions (blue, green and purple arrows) and the metallic region (yellow) are shown. The non-overlapping four-Cu-site plaquettes are shown by black squares with the number '4' inside. The number of Cu sites inside these squares equals N_{4M}. N_M is the number of Cu sites in the metal region (yellow) and N_{Cu} is the total number of Cu sites (here, $N_{Cu} = 20 \times 20 = 400$). For $x < 0.187$, there is enough space to avoid plaquette overlap leading to $N_{4M} = N_M$, as seen in the $x = 0.15$ figure. The Methods section describes how the plaquettes are doped in figure 2.

Prior to describing our detailed model for the anomalous normal state transport, we summarize the cuprate doping phase diagram. All cuprate superconductors have CuO_2 planes. When undoped, they are insulating Heisenberg spin-1/2 antiferromagnets (AF) with a Néel temperature $T_N \sim 200\,K$ and spin–spin coupling $J_{dd} \approx 0.13\,eV$ [5]. The spin is localized on planar Cu atoms in a d^9 configuration with the single unpaired spin in the Cu $d_{x^2-y^2}$ orbital, where the x and y axes point along the Cu—O bonds. Doping of more than $x \approx 0.05$ holes per planar Cu destroys the bulk Néel AF phase and superconductivity occurs for $T < T_c$ where T_c is the superconducting transition temperature. Above T_c, the material is metallic. When x is increased past ≈ 0.27, superconductivity vanishes ($T_c = 0$). The highest T_c occurs for $x \approx 0.16$ [17]. The band structure consists of approximately two-dimensional (2D) CuO_2 bands with Cu $d_{x^2-y^2}$ and O p_σ (p_x and p_y) orbital characters that cross the Fermi level [18]. The Fermi surface is hole-like and centered around $k = (\pi/a, \pi/a)$ where a is the CuO_2 unit cell distance ($a \approx 3.8$ Å).

In our Plaquette model [15], doping creates holes in out-of-the-CuO_2-plane orbitals that are localized in square four-Cu-site plaquettes centered at the dopant. This orbital character was shown by high quality *ab initio* quantum mechanics calculations on $La_{2-x}Sr_xCuO_4$ supercells [19]. These hole orbitals induce delocalization of the four Cu $d_{x^2-y^2}$ and 8 O p_σ orbitals inside the doped plaquette. Each plaquette can be thought of as a tiny piece of metal (see appendix). Recently, x-ray measurements on $La_{2-x}Sr_xCuO_4$ have found evidence of out-of-plane hole character at higher dopings [20].

Figure 3 shows a Sr doped four-Cu-site plaquette (as found in $La_{2-x}Sr_xCuO_4$). In figures 3(a) and (b) the two degenerate out-of-plane states are shown with their respective Jahn–Teller atomic distortions (blue arrows for planar O atoms and black arrows for apical O atoms). In the cuprates, no long-range static distortion compatible with figures 3(a) or (b) is found. Thus the coupling between these out-of-plane hole states is strong, leading to a vibronic or dynamical Jahn–Teller state being formed instead.

Figure 3(c) shows an instantaneous configuration of the out-of-plane holes in a single CuO_2 plane. The out-of-plane hole states are shown by the red 'dumbbells'. Coupling between adjacent plaquettes leads to correlation between the orientations of neighboring dumbbells. When plaquettes overlap as shown by the green squares in figure 3(c), the orbital degeneracy

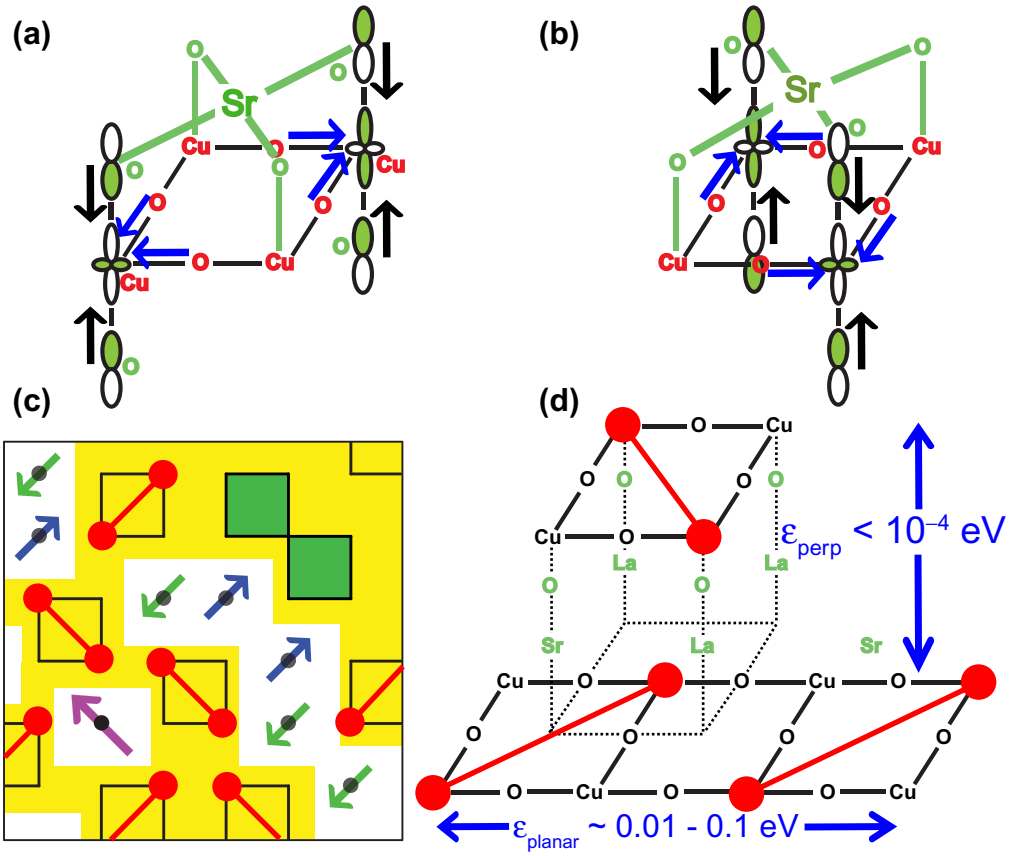

Figure 3. Dynamic Jahn–Teller character of doped plaquettes and their atomic distortions. (a) and (b), the localized out-of-the-CuO_2-plane hole character surrounding a Sr dopant in $La_{2-x}Sr_xCuO_4$. There are two degenerate states. The blue and black arrows show local distortions that stabilize these orbital states. A resonance of these two configurations (a vibronic or dynamic Jahn–Teller effect) occurs. These hole orbitals have Cu d_{z^2} and apical O p_z character (vertical white-green orbitals) that induce the planar Cu $d_{x^2-y^2}$ and O p_σ orbitals inside this plaquette (shown in yellow in (d)) to delocalize over the four-Cu-sites inside the plaquette. When the plaquettes percolate through the crystal (yellow region in (c) and figure 2), a planar Cu/O $d_{x^2-y^2}/p_\sigma$ metallic band is formed inside the yellow region [15, 19] (see appendix). (c) Looking down at a 6×6 square in the CuO_2 plane taken from the upper right corner of $x = 0.19$ doping in figure 2. The red 'dumbbells' show the instantaneous orientation of the out-of-plane orbitals in the square. The degeneracy in (a) and (b) is split in the two overlapping plaquettes in the upper right (green squares). No dynamic Jahn–Teller states are formed there. (d) The coupling energy between neighboring 'dumbbells' inside a CuO_2 plane and between neighboring planes. The coupling energy between planes is very small, $\epsilon_{perp} \sim 3.6 \times 10^{-5}$ eV ~ 0.42 K (see appendix for the calculation). For $T > \epsilon_{perp} \sim 0.42$ K, there is no correlation of the dynamic Jahn–Teller states in adjacent CuO_2 planes. Hence, the phonon modes inside non-overlapping plaquettes lose phase coherence between the planes and become

Figure 3. (Continued) strictly 2D [21, 22]. Within each CuO_2 plane, these modes are amorphous (momentum is not a good quantum number). Amorphous 2D phonons lead to the low-temperature linear T coefficient, $\alpha_1(0)$, as shown in the text.

of the out-of-plane holes shown in figures 3(a) and (b) is removed. Thus overlapping plaquettes have no dynamical Jahn–Teller state.

In figure 3(d), the correlation energy between neighboring dynamical Jahn–Teller states is shown for plaquettes inside a single CuO_2 plane, ϵ_{planar}, and for plaquettes in adjacent CuO_2 planes, ϵ_{perp}. In the appendix, ϵ_{perp} is estimated to be $\sim 3.6 \times 10^{-5}$ eV ~ 0.42 K and ϵ_{planar} is on the order 0.01–0.1 eV ($\sim$100–1000 K).

For temperatures greater than ~ 1 K, there is no correlation between dynamic Jahn–Teller states between planes. In analogy to the 'dynamical detuning' proposed for electron transport normal to the CuO_2 planes [21, 22], the lack of correlation of dynamical Jahn–Teller states normal to the plane disrupts the phase coherence of phonons between CuO_2 layers. Hence, the phonon modes inside non-overlapping plaquettes become strictly 2D for temperatures greater than ϵ_{perp}.

Since momentum is not a good quantum number for the 2D phonon modes inside the region of the non-overlapping plaquettes, these modes have the same character as those in amorphous metals. We show later that these amorphous 2D phonons lead to the low-temperature linear resistivity (the $\alpha_1(0)$ term in figure 1). Also, $\alpha_1(0) \propto N_{4\text{M}}$ because the number of amorphous 2D phonon modes is proportional to the total number of Cu sites inside the non-overlapping four-Cu-site plaquettes, $N_{4\text{M}}$.

The phonon modes occurring 'outside' the non-overlapping plaquettes are amorphous and three-dimensional (3D). The number of these modes is proportional to $N_{\text{Cu}} - N_{4\text{M}}$. These modes lead to the T^2 resistivity term, as we show later.

A percolating pathway of plaquettes leads to a delocalized metallic Cu $d_{x^2-y^2}$ and O p_σ band inside the percolating swath (yellow region in figure 2). The undoped regions (not part of the doped metallic swath) remain localized d^9 Cu spins with AF coupling. Thus cuprates are intrinsically inhomogeneous with a percolating metallic region and insulating AF regions.

Our proposed inhomogeneity appears prima facie to be at odds with the recent observation of quantum oscillations in heavily overdoped Tl-2201 cuprates [23–25]. In the appendix, we estimate the Dingle temperature arising from the inhomogeneity in our model and show that it is compatible with these measurements.

The phonon modes that lead to superconductivity involve the planar displacement of the O atoms at the interface between the metal and AF regions (figures 4 and 5). These longitudinal-optical (LO) O phonon modes are the softened modes seen by neutron scattering [26–28] for the superconducting range of dopings for momenta along the $(\pi, 0)$ and $(0, \pi)$ directions. They are different from the Jahn–Teller modes (figures 3(a) and (b)) that lead to the linear T term in ρ. Figure 6 shows how these modes lead to the observed d-wave ($d_{x^2-y^2}$) superconducting gap.

To complete the derivation of the results in figure 1, we must show that phonon modes inside the non-overlapping plaquettes produce the anisotropic $\cos^2(2\varphi)T$ scattering rate and that the remaining phonons contribute the T^2 isotropic term. In a typical metal with full translational symmetry, the scattering rate for a metallic electron with momentum k is [3] $1/\tau(k) \sim \sum_{k',q} (\hbar/M\omega_q) q^2 (1 - \cos\theta) n_{\text{B}}(\omega_q) \delta(k' - k - q)$ where the sum is over k' on the

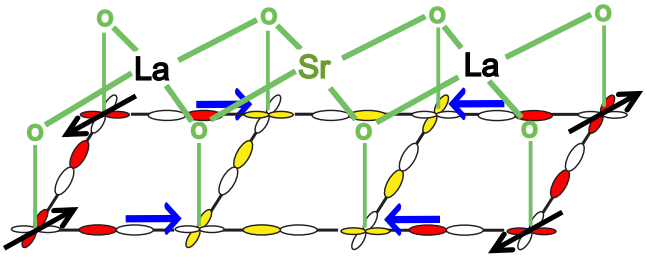

Figure 4. 3D picture of the distortion of the O atoms between the metallic (yellow) and AF (red) regions. These modes are shown in greater detail in figure 5 and lead to d-wave superconductivity as shown in figure 6.

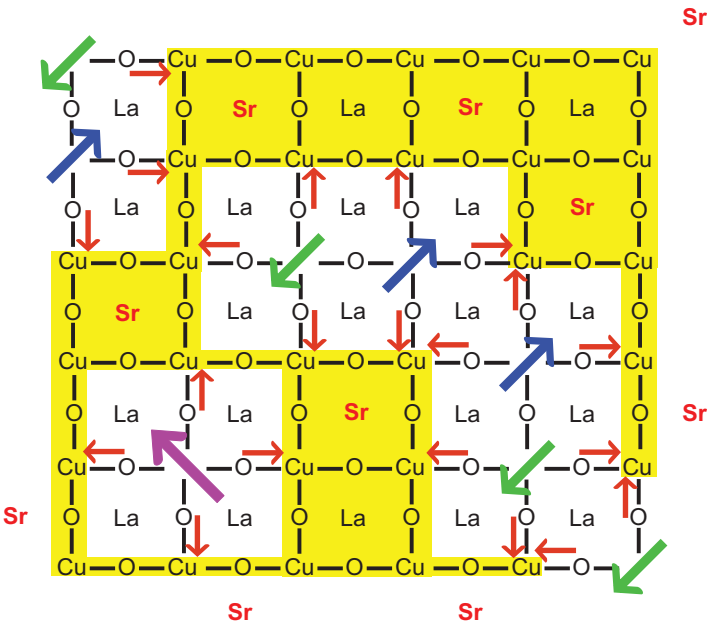

Figure 5. The AF/metal interfacial O phonon modes. Fully expanded 6×6 black square in the upper right corner of $x = 0.19$ doping from figure 2. The interfacial O phonon modes (red arrows) are the origin of the observed softened phonon LO oxygen modes seen by neutron scattering with wavevectors along the Cu—O bond directions [$(0, 0)$ to $(\pi, 0)$ and $(0, \pi)$] for the superconducting range of dopings [26–28]. These modes lead to a d-wave superconducting gap as shown in figure 6.

Fermi surface and q is the phonon momentum. M is the nuclear mass, ω_q is the phonon energy, θ is the angle between k and k' and $n_B(\omega) = 1/(e^{\hbar\omega/k_BT} - 1)$ is the Bose–Einstein distribution (k_B is Boltzmann's constant). The delta function maintains momentum conservation. The $(1 - \cos\theta)$ term becomes T dependent at low T because $n_B(\omega)$ restricts the scattering to small-angles ($\theta \ll 1$).

All phonons can scatter k to k' in cuprates because of their intrinsic inhomogeneity. Hence, the $(1 - \cos\theta)$ term in $1/\tau(k)$ has no T dependence. In this case [29], $1/\tau(k) \sim \sum_{k',\lambda}(\hbar/M\omega_\lambda)(k' - k)^2 n_B(\omega_\lambda)$ where λ is summed over all phonon modes and the delta function

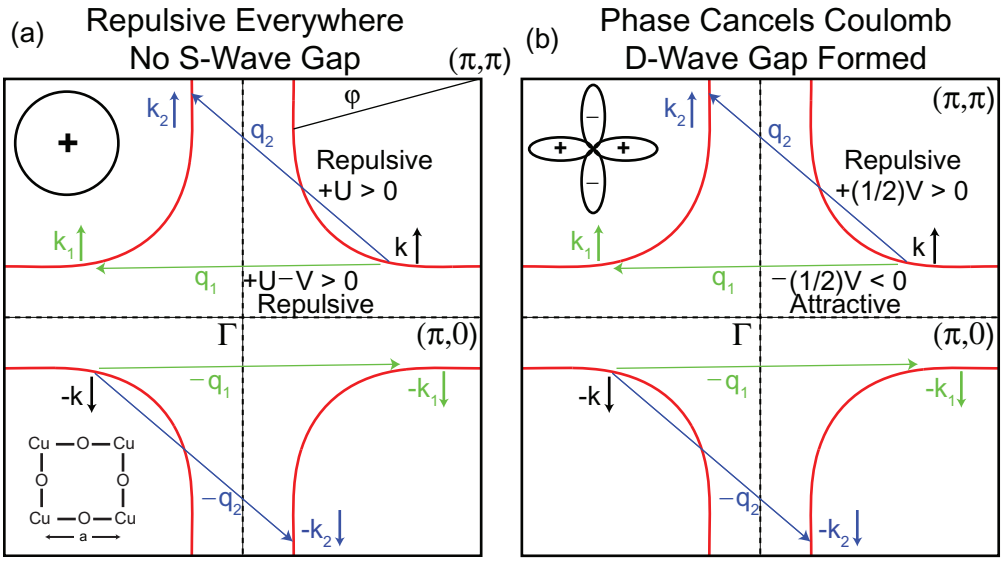

Figure 6. Schematic diagram of the cuprate Fermi surface showing how a strong attractive phonon pairing along the Cu—O bond directions leads to the observed d-wave ($d_{x^2-y^2}$) superconducting gap. Panels (a) and (b) show the hole-like Fermi surface centered at $(\pi/a, \pi/a)$ where $a \approx 3.8$ Å is the unit cell distance (the Γ-point is occupied). The Cu—O unit cell in the lower left corner of (a) shows the orientation of the Brillouin zone relative to the crystal lattice. In both (a) and (b), a $(k\uparrow, -k\downarrow)$ Cooper pair in black is scattered by a phonon with momentum q_1 or q_2 to $(k_1\uparrow, -k_1\downarrow)$ in green and $(k_2\uparrow, -k_2\downarrow)$ in blue, respectively. A Coulomb repulsion, $(+U > 0)$, occurs for both q_1 and q_2. q_1 has an additional phonon-mediated attraction, $-V < 0$, from the AF/metal interfacial O atoms in figures 4 and 5. For an isotropic s-wave gap, there is a net repulsion everywhere (upper left corner of (a)). Superconductivity cannot occur for this gap symmetry. For a $d_{x^2-y^2}$ gap (upper left of (b)), the average coupling around the Fermi surface of $+U - (1/2)V$ integrates to zero leaving a net attractive $-(1/2)V$ pairing along the Cu—O bond directions and a repulsive $+(1/2V)$ coupling for $q \approx (\pi/a, \pi/a)$. A $d_{x^2-y^2}$ gap can lower the energy. Thus the modes in figures 4 and 5 lead to the observed d-wave gap. The idea of a d-wave gap arising from the softened oxygen LO phonon modes along the Cu—O bond directions has been suggested previously [31]. In particular, Phillips [32, 33] argued for softened modes occurring at the interface of the AF and metallic regions. What is new here, is that the physical origin of these phonon modes is provided along with its doping evolution.

has disappeared. The number of excited phonon modes at temperature $T < \Theta_{\text{Debye}}$ is $\sim T^d$ where d is the dimension of the phonon modes [30]. At high T, all phonon modes are excited. At low temperatures, $1/\tau \sim (1/\omega)T^d \sim T^{d-1}$, because $\hbar\omega \sim k_B T$. Our expression for $1/\tau$ is identical to the Debye–Waller factor [3, 30] that appears in the resistivity of amorphous metals (see appendix for details). At high T, $1/\tau \sim T$ because all phonon modes become thermally accessible and the occupation number for each mode, n_B, is proportional to T.

The 2D Jahn–Teller modes in figure 3 have $d = 2$, leading to $1/\tau \sim T$. This linear scattering rate persists for $T > \epsilon_{\text{perp}} \sim 0.4$ K. The remaining 3D modes lead to $1/\tau \sim T^2$. Since the phonon modes are amorphous, $1/\tau(k)$ is independent of k for the 3D T^2 modes. The 2D Jahn–Teller modes are derived from the vibronic distortions in figure 3. These modes raise the Cu orbital energy for two diagonal Cu atoms in a plaquette and lower the orbital energy for the other two Cu atoms. Hence, their scattering is modulated by an envelope function $\approx \cos^2(2\varphi)$. Thus $1/\tau(k) \sim \cos^2(2\varphi)T$. This modulation of $1/\tau(k)$ does not change the total scattering around the Fermi surface. Instead, it merely redistributes its weight around the surface. Hence, the proportionality constant in front of the expressions for $\alpha_1(0)$ and $\alpha_1(\infty)$ is the same.

Thus the doping and temperature dependence of the resistivity of cuprates is due to the intrinsic inhomogeneity of these materials. This inhomogeneity arises from the dopant atoms and leads to a percolating metallic region and insulating AF regions. The percolating metallic region is comprised of four-Cu-site plaquettes that are centered around dopants. The plaquettes may overlap each other. We show that the ratio of non-overlapping plaquettes to the total number of Cu atoms equals the ratio of the low and high temperature linear T terms in the resistivity, $\alpha_1(0)/\alpha_1(\infty)$, with no adjustable parameters. We calculate this ratio and find very good agreement with experiment. The resistivity is shown to be due to phonon scattering. The special 'crossover' doping, $x \approx 0.19$, for $\alpha_1(0)$ and $\alpha_1(\infty)$ occurs at the doping when plaquettes first begin to overlap. We calculate this value to be $x = 0.187$ with no adjustable parameters. The low doping value of $\alpha_1(0)$ and the high doping value of $\alpha_1(\infty)$ are found to be exactly the same in our model. This is observed by experiments within the error bars. We find an excellent fit to the doping evolution of $\alpha_1(0)$ and $\alpha_1(\infty)$ with one adjustable multiplicative constant. We also provide a physical picture for the origin of the observed softened LO O phonon mode and show that it leads to a d-wave superconducting gap.

We conclude that the anomalous normal state transport in cuprates provides strong evidence for intrinsic inhomogeneity, metallic percolation, phonon superconducting pairing and phonon normal state scattering.

1. Methods

We dope plaquettes using a simple model for the Coulomb repulsion of the dopants. Since the dopants reside in the metallic region, the repulsion is screened over a short distance. Thus we assume plaquettes are randomly doped without overlap. This doping is possible up to $x = 0.187$. For $x > 0.187$, it is impossible to add dopants without overlapping another plaquette. Above $x = 0.187$, the most energetically favorable location for a dopant is on a site that dopes three undoped d^9 Cu atoms and one previously doped Cu atom. At $x = 0.226$, it is no longer possible to locate three undoped d^9 Cu atoms that are part of a 4-site square. Hence, two undoped d^9 Cu's and two previously doped Cu's are doped up to $x = 0.271$. At this point, there are no adjacent pairs of d^9 spins. Single undoped d^9 Cu doping occurs up to $x = 0.317$. Above this doping, there are no remaining undoped d^9 Cu's. The green squares in figure 2 show all the plaquettes that overlap another plaquette (share at least one Cu atom). The percolating metallic region has become the whole crystal. We have not computed dopings beyond this value ($x = 0.317$). For the results in figure 1, we doped a $10^3 \times 10^3$ square CuO_2 lattice 10^3 different times. N_{4M}/N_{Cu}, and N_M/N_{Cu} values were obtained by averaging over the ensemble (see figures A.1 and A.2).

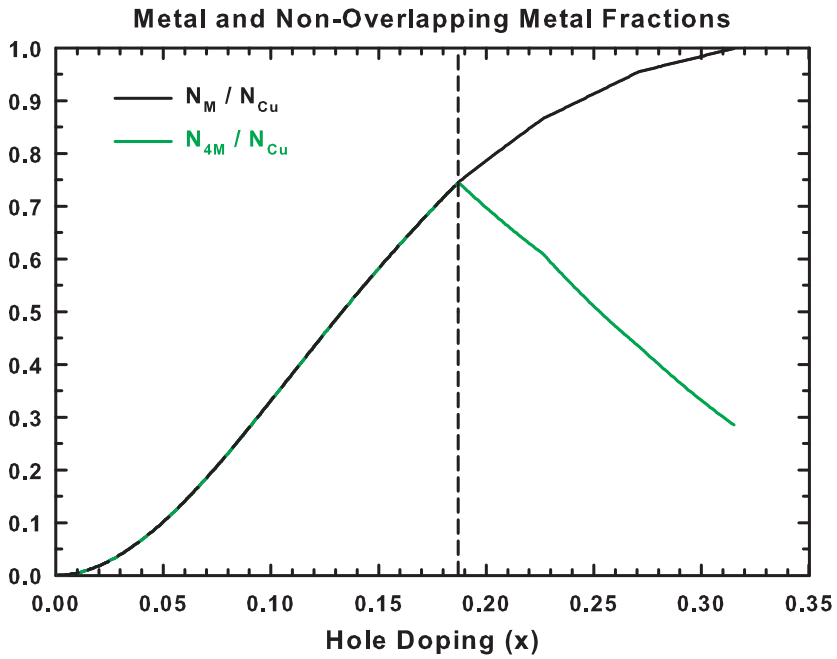

Figure A.1. Calculated N_{M} and $N_{4\mathrm{M}}$ as a fraction of the total number of Cu sites, N_{Cu}. The green curve is exactly the same as $\alpha_1(0)/\alpha_1(\infty)$ in figure 1. The error bars in this figure are smaller than the width of the lines. The algorithm used to compute these curves is described in the Methods section.

Acknowledgments

The author is grateful to Andres Jaramillo–Botero and Carver A Mead for many stimulating discussions. The author also thanks the two referees and Editorial Board Member for their constructive comments.

Appendix A. Metal plaquette counting as a function of doping

Figure A.1 shows the calculated number of Cu atoms inside the metallic region, N_{M}, and the number of metallic Cu atoms that reside in non-overlapping plaquettes, $N_{4\mathrm{M}}$. In figure 2 of the main text, the number of Cu sites in the black squares with '4' inside is $N_{4\mathrm{M}}$ and the yellow region of the same figure is N_{M}. The doping evolution of these two numbers determines the low and high T linear coefficients of the resistivity shown in figure 1 ($\alpha_1(0)$ and $\alpha_1(\infty)$).

Figure A.2 shows the doping evolution of the two different types of non-overlapping plaquettes. Only the non-overlapping plaquettes inside the metallic regions (black squares with '4' inside in figure 2 of the main text) contribute to the low T coefficient of the resistivity ($\alpha_1(0)$). There are additional non-overlapping plaquettes in figure 2 outside of the metallic region. They are shown by red squares in the figure and are isolated plaquettes. The number and spatial distribution of these isolated plaquettes determines the PG and its doping evolution as shown in [15].

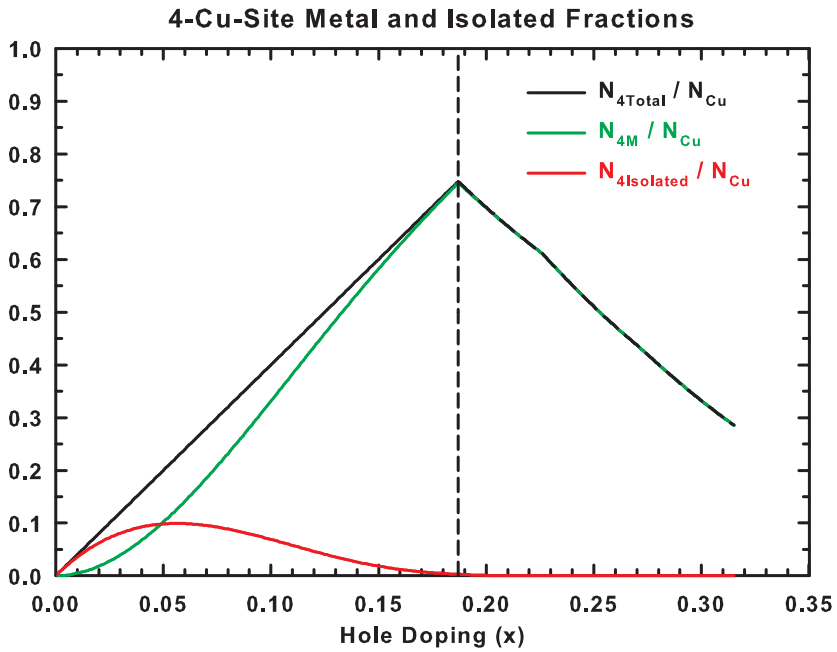

Figure A.2. Doping evolution of the metallic and isolated non-overlapping plaquettes. The green line is the number of Cu sites contained in non-overlapping plaquettes inside the metallic region per planar Cu, N_{4M}/N_{Cu}, and the red line is the number of Cu sites inside the isolated plaquettes per planar Cu, $N_{4Isolated}/N_{Cu}$, appearing as red squares in figure 2. The green line is equal to $\alpha_1(0)/\alpha_1(\infty)$ in figure 1 and is also plotted in A.1. The error bars in this figure are smaller than the width of the lines. The isolated plaquettes are responsible for the PG [15] and are not relevant for the resistivity. The black line is the total number of Cu sites in non-overlapping plaquettes, $N_{4Total} = N_{4M} + N_{4Isolated}$. For $x < 0.187$, there is no plaquette overlap leading to $N_{4Total}/N_{Cu} = 4x$. For $x > 0.187$, $N_{4Isolated} \to 0$ very rapidly, leading to $N_{4M} \to N_{4Total}$.

Appendix B. Cu/O $d_{x^2-y^2}/p_\sigma$ band delocalization inside the metallic region

Figure B.1 shows the shift in the orbital energy of the metallic Cu $d_{x^2-y^2}$ orbital and the neighboring O p_σ orbital due to the dopant induced localized out-of-plane hole. Since the $d_{x^2-y^2}$ orbital energy is lowered more than p_σ, delocalization can occur, leading to a Cu/O $d_{x^2-y^2}/p_\sigma$ band inside the percolating metallic region. Further details are provided in [15] and its supplementary information.

Appendix C. *Ab initio* density functional theory calculations on $La_{2-x}Sr_xCuO_4$ supercells

Pure density functionals such as local density approximation (LDA) [18, 34, 35] and gradient-corrected functionals (generalized gradient approximation (GGA), Perdew–Burke–Ernzerhof (PBE), etc) [36] obtain a metallic ground state for the undoped cuprates rather than an AF insulator because they underestimate the band gap due to a derivative discontinuity of the energy with respect to the number of electrons [37, 38]. In essence, the LDA and PBE functionals

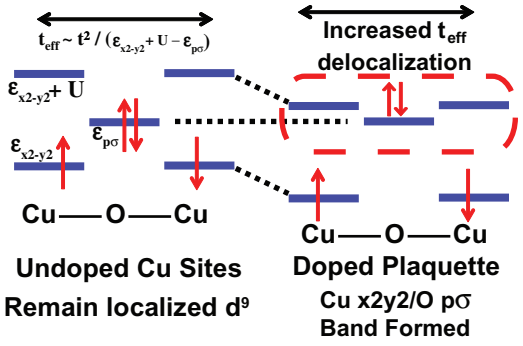

Figure B.1. Delocalization of Cu $d_{x^2-y^2}$/O p_σ electrons inside four-Cu-site doped plaquette [15, 19]. The additional hole induced by substituting Sr for La does not go into the planar Cu $d_{x^2-y^2}$/O p_σ orbitals as is usually assumed. Instead, it is comprised of predominantly apical O p_z and Cu d_{z^2} as seen in figure 3 of the main text. The planar Cu sites surrounding the Sr dopant are called doped sites. Planar Cu sites that are not in the vicinity of a dopant (only La nearby) are called undoped sites. The energy level diagram shows how an out-of-plane hole above the planar Cu sites leads to delocalization of the d^9 Cu spins and the formation of delocalized Cu $d_{x^2-y^2}$/O p_σ states inside the plaquette. The left figure shows the energy levels that occur at undoped Cu sites where there are no holes in out-of-the-plane orbitals. In this case, the difference in energy between the doubly occupied Cu site and the planar O orbital energy, $\epsilon_{x^2-y^2} + U - \epsilon_p$, is large, leading to localization of spins on the Cu. In the right figure, the Cu orbital energy is reduced due to the missing electron in the apical O sites directly above the Cu atoms leading to the neighboring doubly occupied O p_σ electrons delocalizing onto the Cu sites. When two plaquettes are neighbors, the delocalization occurs over all eight Cu sites. When the doping is large enough that the plaquettes percolate in 3D through the crystal, a 'metallic' band is formed in the percolating swath and current can flow from one end of the crystal to the other. This metallic band carries the current in the normal state and becomes superconducting below T_c.

include too much self-Coulomb repulsion. This repulsion leads to more delocalized electronic states. Removing this extra repulsion is necessary in order to obtain the correct localized AF spin states of the undoped cuprates.

The self-repulsion problem with LDA has been known for a long time [39]. Very soon after the failure of LDA to obtain the undoped insulating antiferromagnet for cuprates, several approaches were applied to correct the flaws in LDA for La_2CuO_4. Using a self-interaction-corrected method [39] (SIC-LDA) [40], Svane achieved spin localization with an indirect band gap of 1.04 eV, and Temmerman *et al* [41] found a band gap of 2.1 eV. Using an LDA + U method, Czyzyk and Sawatzky [42] obtained 1.65 eV. In all of these calculations on the undoped cuprates, an increase in out-of-plane orbital character was noted in states just below the top of the valence band. Calculations with explicit dopants such as Sr in $La_{2-x}Sr_xCuO_4$ were not done.

Our *ab initio* calculations [19, 43] were performed using the hybrid density functional, B3LYP. Due to its remarkable success on molecular systems, B3LYP has been the workhorse

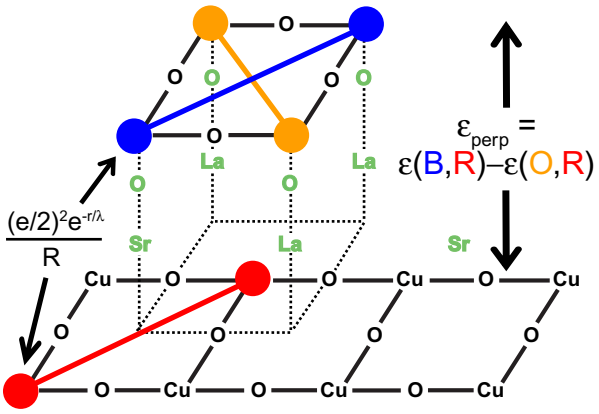

Figure B.2. Estimating the coupling between dynamic Jahn–Teller modes in neighboring CuO_2 planes. The coupling, $\epsilon_{\rm perp}$, is given by the difference in Coulomb repulsion energy between the blue and red 'dumbbells', $\epsilon(B, R)$, and the orange and red 'dumbbells', $\epsilon(O, R)$. The $1/R$ Coulomb repulsion is attenuated by the Thomas–Fermi metallic screening length (derived in the text to be, $\lambda \approx 0.69$ Å). Since the charge in a dumbbell is divided equally between the two ends, a charge of $(1/2)e$ is used for each interaction term (e is the electron charge). The Cu–Cu lattice spacing in the plane is 3.8 Å and the distance between planes is 6.0 Å. We find $\epsilon_{\rm perp} = 3.6 \times 10^{-5}$ eV $= 0.42$ K.

density functional for molecular chemistry computations for almost 20 years [44, 45]. For example [44], B3LYP has a mean absolute deviation (MAD) of 0.13 eV, LDA MAD = 3.94 eV and PBE MAD = 0.74 eV for the heats of formation, $\Delta H_{\rm f}$, of the 148 molecules in the extended G2 set [46, 47]. B3LYP has also been found to predict excellent band gaps for carbon nanotubes and binary and ternary semiconductors relevant to photovoltaics and thermoelectrics [48, 49].

The essential difference between B3LYP and all pure density functionals is that 20% exact Hartree–Fock (HF) exchange is included. B3LYP is called a hybrid functional because it includes exact HF exchange. The HF exchange removes some of the self-Coulomb repulsion of an electron with itself found in pure density functional theory functionals. A modern viewpoint of the reason for the success of hybrid functionals is that inclusion of some exact HF exchange compensates the error for fractional charges that occur in LDA, PBE, and other pure density functionals [50]. The downside to using hybrid functionals is they are computationally more expensive than pure density functionals.

Our B3LYP calculations reproduced the experimental 2.0 eV band gap for undoped La_2CuO_4 and also had very good agreement for the AF spin–spin coupling, $J_{dd} = 0.18$ eV (experiment is ≈ 0.13 eV) [43]. We also found substantial out-of-plane apical O p_z and Cu d_{z^2} character near the top of the valence band in agreement with LDA + U and SIC-LDA calculations.

We also performed B3LYP calculations on $La_{2-x}Sr_xCuO_4$ for $x = 0.125$, 0.25 and 0.50 with explicit Sr atoms using large supercells [19]. Regardless of the doping value, we always found that the Sr dopant induces a localized hole in an out-of-the-plane orbital that is delocalized over the four-site region surrounding the Sr as shown in figures 3 and B.1. This result is in contrast to removing an electron from the planar Cu $d_{x^2-y^2}$/O p_σ as predicted by LDA and PBE.

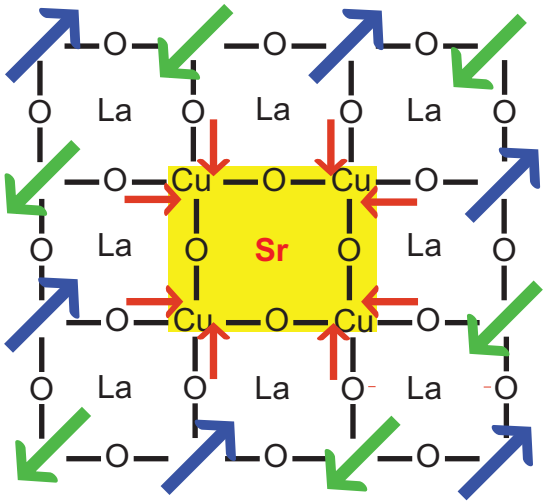

Figure B.3. Oxygen phonon mode around an isolated plaquette. The figure zooms into the 4×4 dotted black square in the lower right corner of the $x = 0.19$ doping in figure 2. The yellow here denotes the isolated plaquette (shown by a red square in figure 2). Yellow is used here to signify that there is delocalization of the Cu/O $d_{x^2-y^2}p_\sigma$ orbitals inside the plaquette. Since this plaquette is not connected to any other plaquette, these electronic states remain localized inside the plaquette. An orbital degeneracy at the Fermi energy of these electronic states leads to the PG [15]. The O atoms that reside between the localized spins in the AF region and the delocalized electronic states inside the plaquettes will distort and the energy of this mode will change. We show the phonon mode by red arrows.

Our calculations found that the apical O's in the doped CuO_6 octahedron are asymmetric anti-Jahn–Teller distorted. In particular, the O atom between the Cu and Sr is displaced 0.24 Å while the O atom between the Cu and La is displaced 0.10 Å. XAFS measurements [51] find the apical O displacement in the vicinity of a Sr to be ≈ 0.2 Å.

Appendix D. Compatibility of our proposed inhomogeneity and quantum oscillations in overdoped Tl-2201

De Haas–van Alphen quantum oscillations have recently been observed in heavily overdoped Tl-2201 [23–25]. These authors concluded that there in no microscopic inhomogeneity in the CuO_2 planes over a minimum of 1200 Å. Hence, these experiments appear to contradict our model of microscopic inhomogeneity in the CuO_2 planes.

Here, we estimate the amount of scattering to be expected from the inhomogeneity in our model and show it is compatible with the data in Rourke *et al* [23]. Rourke *et al* find quantum oscillations in three of the approximately 100 samples tested. Two of samples showing oscillations had doping at ≈ 0.31 doping and the remaining one had doping at ≈ 0.26. Significantly, no samples with lower doping showed quantum oscillations.

Using the doping methodology described in the Methods section of our paper, we find that 4.5% of the planar Cu atoms are localized d^9 spins at 0.26 doping and 0.6% of the planar Cu

atoms are localized d^9 spins at 0.31 doping. At these two dopings, only isolated d^9 spins remain in our model. Below ≈ 0.26 doping, some of the d^9 Cu spins neighbor other d^9 Cu spins. These d^9 Cu atoms are no longer isolated.

In his classic book, Shoenberg [52] states that Dingle temperatures much above 5 K smear out quantum oscillations so that they are not resolvable (p 62). Shoenberg also states (p 62 and table 8.1) that every 1% impurity typically adds 10–100 K to the Dingle temperature. Thus it is possible the $\approx 0.6\%$ 'impurities' we expect for the 0.31 doped samples may still lead to observable quantum oscillations, but the 4.5% impurities at 0.26 doping appears to be too large to be compatible with experiment.

The flaw in the above simplified analysis is that a localized Cu d^9 'impurity' is not a typical impurity. The charge distribution around a metallic and localized d^9 Cu are virtually identical in the CuO_2 planes in cuprates. For both Cu atoms, the Cu has approximately +2 charge with a hole in the $d_{x^2-y^2}$ orbital. The d^9 Cu impurity is not a charged impurity. Instead, it is a neutral impurity with exactly the same sized valence orbitals as the metallic Cu atom. Since the impurity scattering cross section (and hence the scattering length) scales as the square of the difference in the potential between these two types of Cu atoms, the scattering can be up to two orders of magnitude smaller than a typical impurity, as we show below. Thus 4.5% d^9 Cu impurities may lead to the same amount of scattering as 0.045% atomic substitutions of different atoms. At 10–100 K Dingle temperature per 1% impurity, this leads to a Dingle temperature of 0.45–4.5 K for the 0.26 doped sample.

We can use the Friedel sum rule [3] to quantify this physical argument. The Friedel sum rule incorporates the response of the metallic electrons around an impurity to screen out the impurity charge distribution and maintain a constant Fermi energy throughout the crystal. The relevant Cu orbitals near the Fermi level are $d_{x^2-y^2}$, d_{z^2} and 4s with symmetries B_{1g}, A_{1g} and A_{1g}, respectively. The charge difference between the impurity Cu atom and the metallic Cu atom is $Z = 0$, leading to $Z = 0 = \frac{2}{\pi}[\delta_A + \delta_B]$ where δ_B is the $d_{x^2-y^2}$ phase shift at the Fermi level and δ_A is the combined d_{z^2} and 4s phase shifts at the Fermi level. Since there is predominantly $d_{x^2-y^2}$ character at the Fermi level, the d_{z^2} and 4s phase shifts should be small, $\delta_A \sim 0.1$.

The Friedel sum rule therefore forces the $d_{x^2-y^2}$ phase shift to be small, $\delta_B \sim 0.1$ rather than a $\delta_B \sim 1$ for a 'standard' impurity arising from atomic substitution.

Since the scattering cross section scales as $\sin^2\delta_B$ [3], the scattering cross section may be two orders of magnitude smaller than a typical impurity. Thus we have shown that the scattering length expected from the inhomogeneity of our plaquette model leads to Dingle temperatures from 0.45–4.5 K at 0.26 doping and 0.006–0.6 K at 0.31 doping.

Rourke *et al* measure the attenuation of the oscillations due to the Dingle temperature, but they do not quote their Dingle temperature. We can extract their Dingle temperature in two ways.

Firstly, the Dingle temperature, x_D, is given by

$$k_B x_D = \frac{\hbar}{2\pi\tau}, \tag{D.1}$$

where k_B is Boltzmann's constant and τ is the scattering time. Multiplying the top and bottom of the right-hand side of this equation by the Fermi velocity, v_F, we obtain

$$k_B x_D = \frac{\hbar v_F}{2\pi l_0}, \tag{D.2}$$

where l_0 is the scattering length. $l_0 = 400\,\text{Å}$ in Rourke *et al* $v_F \approx 1 - 3 \times 10^7\,\text{cm}\,\text{s}^{-1}$ in cuprates [12]. For $v_F = 2 \times 10^7\,\text{cm}\,\text{s}^{-1}$, $x_D = 6.1\,\text{K}$.

Secondly, we may use

$$k_B x_D = \left(\frac{m_{\text{elec}}}{m_{\text{therm}}}\right)\left(\frac{2\mu_B}{2\pi}\right)\left(\frac{2\hbar F_0}{e}\right)^{1/2}\left(\frac{1}{l_0}\right), \tag{D.3}$$

where $m_{\text{therm}}/m_{\text{elec}}$ is the ratio of the band electron mass measured by the temperature dependence of the oscillation amplitude (∼5 in Rourke *et al*), μ_B is the Bohr magneton, F_0 is the oscillation frequency (1.8×10^4 tesla in Rourke *et al*). This leads to $x_D = 5.2\,\text{K}$.

Therefore, estimates of the scattering from our plaquette induced inhomogeneity lead to a Dingle temperature compatible with observations.

In our model, below ≈ 0.26 doping, there are d^9 Cu atoms that are no longer isolated. These Cu atoms form AF regions in the material. We anticipate that the scattering from these 'non-isolated' regions will lead to greater scattering than isolated d^9 Cu atoms. This may explain why no quantum oscillations were found for dopings less than ≈ 0.26. Despite the calculations done here, further work needs to be done to obtain precise numbers for the scattering cross section from an isolated d^9 Cu spin. What we have shown here is that it is most likely that the inhomogeneity we propose in this paper does not contradict the quantum oscillations found in heavily overdoped Tl-2201.

Appendix E. The Debye–Waller factor and amorphous/glassy metals

For liquid metals, Ziman and Faber [53, 54] showed that the T dependence of the structure factor, $S(K)$, evaluated at $K = 2k_F$, where k_F is the Fermi momentum determines the T dependence of the resistivity. Their resistivity expression is given by [30, 53]

$$\rho(T) = \frac{12\pi\Omega}{e^2\hbar v_F^2}\int_0^1 \mathrm{d}\left(\frac{K}{2k_F}\right)\left(\frac{K}{2k_F}\right)^3 S(K,T)|t(K)|^2. \tag{E.1}$$

Here v_F is the Fermi velocity, $t(K)$ is the scattering matrix element and Ω is the volume.

The integral for ρ is dominated by the maximum momentum transfer across the Fermi surface, or $2k_F$. Thus the T dependence of the structure factor, $S(2k_F, T)$, determines the temperature dependence of ρ.

In amorphous/glassy metals, the structure factor is dominated by the 'zero-phonon' elastic term that is given by $S(K,T) = S(K)e^{-2W(K)}$ where $S(K)$ is the static structure factor and $W(K)$ is the Debye–Waller factor arising from the nuclear motion at temperature T [55–58]. Here, $K = 2k_F$. Using $S(K,T) \approx S(K)[1 - 2W(K)]$, we conclude that the temperature dependence of the $W(K)$ determines the temperature dependence of $\rho(T)$.

The Debye–Waller factor is given by $W(K) = (1/2)\sum_q |K \cdot U_q|^2$ where the sum is over all phonon modes q and U_q is the amplitude for the q mode. U_q can be determined from $(1/2)M\omega_q^2|U_q|^2 \sim (1/2)n(\omega)\hbar\omega_q$ [3] where M is the nuclear mass, $\hbar\omega_q$ is the energy of the phonon mode q and n_q is the Bose–Einstein occupancy of the phonon mode, $n_q = 1/(e^{\beta\hbar\omega_q} - 1)$. From this expression, we find the form of the Debye–Waller factor to be

$$W(K) \sim K^2 \int \frac{n_q}{\omega_q}\mathrm{d}^3q. \tag{E.2}$$

The expression for $W(K)$ has exactly the same form that we obtained from the matrix element argument in the main text [29].

The Bose–Einstein occupation, n_q, cuts off the integral at $\sim k_B T$, where k_B is Boltzmann's constant. Since $\omega_q = cq$, where c is the speed of sound, $W(K) \sim T^2$. For 2D phonon modes, the integral is over d^2q instead of d^3q leading to $W(K) \sim T$.

For 2D, the Debye–Waller factor diverges as $\int d\omega/\omega \sim \log T$ as $T \to 0$. In fact, the 2D phonon modes are not strictly 2D for $T < \epsilon_{perp} \sim 0.4$ K. Less than 0.1 K, these modes are 3D leading to a finite value for the Debye–Waller factor. For $T > 0.1$ K, the Debye–Waller factor is linear in T leading to a linear resistivity.

Appendix F. Estimating the coupling energy of dynamical Jahn–Teller plaquettes in neighboring CuO_2 planes

The coupling energy, ϵ_{perp}, between two dynamical Jahn–Teller plaquettes in adjacent planes is given by the Coulomb repulsion energy difference between the different orientations of the plaquette hole orbitals. The details of the energy difference expression are shown in figure B.2.

The Thomas–Fermi screening length, λ, is estimated from the expression [3]

$$\frac{1}{\lambda^2} = 4\pi e^2 N(0), \tag{F.1}$$

where e is the electron charge and $N(0)$ is the density of states. There is approximately one metallic electron per unit cell leading to a density of states of approximately one state per eV per unit cell. The volume of the unit cell is, $\Omega_{cell} = a^2 d$, where $a = 3.8$ Å and $d = 6.0$ Å. Therefore, $N(0) \approx 87.0\,\text{eV}^{-1}\,\text{Å}^{-3}$ and $\lambda = 0.69$ Å.

Substituting these numbers into the expression shown in figure B.2 leads to $\epsilon_{perp} = 3.6 \times 10^{-5}$ eV $= 0.42$ K.

The above estimate assumes the dielectric constant, $\epsilon_\infty = 1$. In cuprates, the dielectric constant is $\epsilon_\infty \sim 3$–6 [59]. Including ϵ_∞ above increases λ by $\sqrt{\epsilon_\infty}$ and reduces the $1/r$ Coulomb term to $1/\epsilon_\infty r$. We find $\epsilon_{perp} = 6.3$ and 12.7 K for $\epsilon_\infty = 3$ and 6, respectively. Using the Bloch–Gruneisen expression for phonon resistivity in normal metals [3] suggests that a linear in T resistivity will persist down to $\sim \epsilon_{perp}/4 \approx 3.2$ K for $\epsilon_\infty = 6$.

We have chosen $\epsilon_\infty = 1$ because the dynamical Jahn–Teller plaquettes fluctuate rapidly on a timescale given by $\hbar/\epsilon_{planar} \sim 10^{-14}$ s, due to their strong planar coupling with neighboring Jahn–Teller plaquettes. This high frequency fluctuation will reduce the effective dielectric constant from the ϵ_∞ values above.

Appendix G. Oxygen modes around an isolated (red) plaquette

The red arrows in figure B.3 show the softened phonon mode for the O atoms between the AF spins and the delocalized electrons inside the isolated plaquette.

References

[1] Hussey N E *et al* 2011 Dichotomy in the T-linear resistivity in hole-doped cuprates *Phil. Trans. R. Soc.* A **369** 1626–39

[2] Gurvitch M and Fiory A T 1987 Resistivity of $La_{1.825}Sr_{0.175}CuO_4$ and $YBa_2Cu_3O_7$ to 1100 K—absence of saturation and its implications *Phys. Rev. Lett.* **59** 1337–40

[3] Ziman J M 1972 *Principles of the Theory of Solids* 2nd edn (Cambridge: Cambridge University Press)

[4] Decroux M *et al* 1987 Structure, resistivity, critical-field, specific-heat jump at T_c, Meissner effect, ac and dc susceptibility of the high-temperature superconductor $La_{2-x}Sr_xCuO_4$ *Europhys. Lett.* **3** 1035–40
[5] Sulewski P E, Fleury P A, Lyons K B, Cheong S W and Fisk Z 1990 Light-scattering from quantum spin fluctuations in La_2CuO_4, Nd_2CuO_4, Sm_2CuO_4 *Phys. Rev.* B **41** 225–30
[6] Hussey N E, Takenaka K and Takagi H 2004 Universality of the Mott–Ioffe–Regel limit in metals *Phil. Mag.* **84** 2847–64
[7] Emery V J and Kivelson S A 1995 Superconductivity in bad metals *Phys. Rev. Lett.* **74** 3253–6
[8] Ando Y 2008 Implication of the Mott-limit violation in high-T_c cuprates *J. Phys. Chem. Solids* **69** 3195–8
[9] Abdel-Jawad M *et al* 2006 Anisotropic scattering and anomalous normal-state transport in a high-temperature superconductor *Nature Phys.* **2** 821–5
[10] Analytis J G, Abdel-Jawad M, Balicas L, French M M J and Hussey N E 2007 Angle-dependent magnetoresistance measurements in $Tl_2Ba_2CuO_{6+\delta}$ and the need for anisotropic scattering *Phys. Rev.* B **76** 104523
[11] Cooper R A *et al* 2009 Anomalous criticality in the electrical resistivity of $La_{2-x}Sr_xCuO_4$ *Science* **323** 603–7
[12] Hussey N E 2003 The normal state scattering rate in high-T_c cuprates *Eur. Phys. J.* B **31** 495–507
[13] Kokalj J, Hussey N E and McKenzie R H 2012 Transport properties of the metallic state of overdoped cuprate superconductors from an anisotropic marginal fermi liquid model *Phys. Rev.* B **86** 045132
[14] Naqib S H, Cooper J R, Tallon J L and Panagopoulos C 2003 Temperature dependence of electrical resistivity of high-T_c cuprates—from pseudogap to overdoped regions *Physica* C **387** 365–72
[15] Tahir-Kheli J and Goddard W A 2011 Origin of the pseudogap in high-temperature cuprate superconductors *J. Phys. Chem. Lett.* **2** 2326–30
[16] Tahir-Kheli J and Goddard W A 2010 Universal properties of cuprate superconductors: T_c phase diagram, room-temperature thermopower, neutron spin resonance, and STM incommensurability explained in terms of chiral plaquette pairing *J. Phys. Chem. Lett.* **1** 1290–5
[17] Tallon J L, Bernhard C, Shaked H, Hitterman R L and Jorgensen J D 1995 Generic superconducting phase-behavior in high-T_c cuprates—T_c variation with hole concentration in $YBa_2Cu_3O_{7-\delta}$ *Phys. Rev.* B **51** 12911–4
[18] Pickett W E 1989 Electronic-structure of the high-temperature oxide superconductors *Rev. Mod. Phys.* **61** 433–512
[19] Perry J K, Tahir-Kheli J and Goddard W A 2002 *Ab initio* evidence for the formation of impurity $d_{3z^2-r^2}$ holes in doped $La_{2-x}Sr_xCuO_4$ *Phys. Rev.* B **65** 144501
[20] He R-H *et al* 2013 Observation of symmetry-distinct states proximate to the Fermi level in a, high-T_c cuprate family *Bull. Am. Phys. Soc.* **58** http://meetings.aps.org/link/BAPS.2013.MAR.F35.3
[21] Leggett A J 1992 Some aspects of the c-axis coupling and transport in the copper oxide superconductors *Braz. J. Phys.* **22** 129–39
[22] Turlakov M and Leggett A J 2001 Interlayer *c*-axis transport in the normal state of cuprates *Phys. Rev.* B **63** 064518
[23] Rourke R M C *et al* 2010 A detailed de Haas–van Alphen effect study of the overdoped cuprate $Tl_2Ba_2CuO_{6+\delta}$ *New J. Phys.* **12** 105009
[24] Vignolle B *et al* 2008 Quantum oscillations in an overdoped high-T_c superconductor *Nature* **455** 952–5
[25] Bangura A F *et al* 2010 Fermi surface and electronic homogeneity of the overdoped cuprate superconductor $Tl_2Ba_2CuO_{6+\delta}$ as revealed by quantum oscillations *Phys. Rev.* B **82** R104501
[26] Pintschovius L, Reznik D and Yamada K 2006 Oxygen phonon branches in overdoped $La_{1.7}Sr_{0.3}Cu_3O_4$ *Phys. Rev.* B **74** 174514
[27] Reznik D *et al* 2006 Electron–phonon coupling reflecting dynamic charge inhomogeneity in copper oxide superconductors *Nature* **440** 1170–3
[28] Pintschovius L 2005 Electron–phonon coupling effects explored by inelastic neutron scattering *Phys. Status Solidi* b **242** 30–50

[29] Bergmann G 1971 Eliashberg function $\alpha^2(\epsilon)F(\epsilon)$ and strong-coupling behavior of a disordered superconductor *Phys. Rev.* B **3** 3797–801
[30] Cote P and Meisel L 1981 *Glassy Metals I* (*Topics in Applied Physics* vol 46) ed H-J Guntherodt and H Beck (Berlin: Springer) pp 141–66
[31] Phillips J C 2003 Nanoscopic filters as the origin of d-wave energy gaps *Phil. Mag.* **83** 3255–65
[32] Phillips J C 1989 *Physics of High-T_c Superconductors* (San Diego, CA: Academic)
[33] Phillips J C 2007 Self-organized networks and lattice effects in high-temperature superconductors *Phys. Rev.* B **75** 214503
[34] Yu J J, Freeman A J and Xu J H 1987 Electronically driven instabilities and superconductivity in the layered $La_{2-x}Ba_xCuO_4$ perovskites *Phys. Rev. Lett.* **58** 1035–7
[35] Mattheiss L F 1987 Electronic band properties and superconductivity in $La_{2-y}X_yCuO_4$ *Phys. Rev. Lett.* **58** 1028–30
[36] Perry J K, Tahir-Kheli J and Goddard W A 2001 unpublished
[37] Perdew J P and Levy M 1983 Physical content of the exact Kohn–Sham orbital energies—band-gaps and derivative discontinuities *Phys. Rev. Lett.* **51** 1884–7
[38] Sham L J and Schluter M 1983 Density-functional theory of the energy-gap *Phys. Rev. Lett.* **51** 1888–91
[39] Perdew J P and Zunger A 1981 Self-interaction correction to density-functional approximations for many-electron systems *Phys. Rev.* B **23** 5048–79
[40] Svane A 1900 Electronic-structure of La_2CuO_4 in the self-interaction-corrected density functional formalism *Phys. Rev. Lett.* **68** 1900–3
[41] Temmerman W M, Szotek Z and Winter H 1993 Self-interaction-corrected electronic-structure of La_2CuO_4 *Phys. Rev.* B **47** 11533–6
[42] Czyzyk M T and Sawatzky G A 1994 Local-density functional and on-site correlations—the electronic-structure of La_2CuO_4 and $LaCuO_3$ *Phys. Rev.* B **49** 14211–28
[43] Perry J K, Tahir-Kheli J and Goddard W A 2001 Antiferromagnetic band structure of La_2CuO_4: Becke-3-Lee–Yang–Parr calculations *Phys. Rev.* B **63** 144510
[44] Xu X and Goddard W A 2004 The X3LYP extended density functional for accurate descriptions of non-bond interactions spin states and thermochemical properties *Proc. Natl Acad. Sci. USA* **101** 2673–7
[45] Bryantsev V S, Diallo M S, van Duin A C T and Goddard W A 2009 Evaluation of B3LYP, X3LYP, and M06-class density functionals for predicting the binding energies of neutral, protonated, and deprotonated water clusters *J. Chem. Theory Comput.* **5** 1016–26
[46] Curtiss L A, Raghavachari K, Trucks G W and Pople J A 1991 Gaussian-2 theory for molecular-energies of 1st-row and 2nd-row compounds *J. Chem. Phys.* **94** 7221–30
[47] Curtiss L A, Raghavachari K, Redfern P C and Pople J A 1997 Assessment of Gaussian-2 and density functional theories for the computation of enthalpies of formation *J. Chem. Phys.* **106** 1063–79
[48] Matsuda Y, Tahir-Kheli J and Goddard W A 2010 Definitive band gaps for single-wall carbon nanotubes *J. Phys. Chem. Lett.* **1** 2946–50
[49] Xiao H, Tahir-Kheli J and Goddard W A 2011 Accurate band gaps for semiconductors from density functional theory *J. Phys. Chem. Lett.* **2** 212–7
[50] Mori-Sanchez P, Cohen A J and Yang W T 2008 Localization and delocalization errors in density functional theory and implications for band-gap prediction *Phys. Rev. Lett.* **100** 146401
[51] Haskel D, Stern E A, Hinks D G, Mitchell A W and Jorgensen J D 1997 Altered Sr environment in $La_{2-x}Sr_xCuO_4$ *Phys. Rev.* B **56** R521–4
[52] Shoenberg D 1984 *Magnetic Oscillations in Metals* (Cambridge: Cambridge University Press)
[53] Ziman J M A 1961 Theory of the electrical properties of liquid metals—the monovalent metals *Phil. Mag.* **6** 1013–34
[54] Faber T E and Ziman J M 1965 A theory of electrical properties of liquid metals III. resistivity of binary alloys *Phil. Mag.* **11** 153

[55] Nagel S R 1977 Temperature-dependence of resistivity in metallic glasses *Phys. Rev.* B **16** 1694–8
[56] Frobose K and Jackle J 1977 On the temperature dependence of the electrical resistivity of amorphous metals *J. Phys. F: Met. Phys.* **7** 2331–48
[57] Cote P J and Meisel L V 1978 Origin of saturation effects in electron transport *Phys. Rev. Lett.* **40** 1586–9
[58] Meisel L V and Cote P J 1977 Structure factors in amorphous and disordered harmonic Debye solids *Phys. Rev.* B **16** 2978–80
[59] Tanner D B and Timusk T 1992 *Physical Properties of High Temperature Superconductors III* ed D M Ginsberg (Singapore: World Scientific) pp 363–469